

# Design, simulation and characterization of integrated photonic spectrographs for Astronomy I: Generation-I AWG devices based on canonical layouts

ANDREAS STOLL,<sup>1,\*</sup> KALAGA V. MADHAV,<sup>1</sup> AND MARTIN M. ROTH<sup>1</sup>

<sup>1</sup>Leibniz-Institut für Astrophysik (AIP), An der Sternwarte 16, 14482 Potsdam, Germany  
\*astoll@aip.de

**Abstract:** We present an experimental study on our first generation of custom-developed arrayed waveguide gratings (AWG) on silica platform for spectroscopic applications in near-infrared astronomy. We provide a comprehensive description of the design, numerical simulation and characterization of several AWG devices aimed at spectral resolving powers of 15,000 - 60,000 in the astronomical H-band. We evaluate the spectral characteristics of the fabricated devices in terms of insertion loss and estimated spectral resolving power and compare the results with numerical simulations. We estimate resolving powers of up to 18,900 from the output channel 3-dB transmission bandwidth. Based on the first characterization results, we select two candidate AWGs for further processing by removal of the output waveguide array and polishing the output facet to optical quality with the goal of integration as the primary diffractive element in a cross-dispersed spectrograph. We further study the imaging properties of the processed AWGs with regards to spectral resolution in direct imaging mode, geometry-related defocus aberration, and polarization sensitivity of the spectral image. We identify phase error control, birefringence control, and aberration suppression as the three key areas of future research and development in the field of high-resolution AWG-based spectroscopy in astronomy.

© 2021 Optical Society of America under the terms of the [OSA Open Access Publishing Agreement](#)

## 1. Introduction

Compact, low-cost optical instruments play an increasingly important role in scientific disciplines ranging from biomedical research to space exploration. In astronomy, the idea of an integrated photonic spectrograph is particularly appealing for space telescopes, where mass and volume are critical parameters for all subsystems of a mission. For example, the NIRSPEC spectrograph onboard the next generation space telescope JWST [1], whose main science cases are (1) cosmology in the epoch of reionization, (2) the assembly of galaxies, (3) the birth of stars and protoplanetary systems, and (4) exoplanets and the origin of life, offers a spectral resolving power of up to  $R = 2700$  in three wavelength bands between  $1\ \mu\text{m}$  and  $5\ \mu\text{m}$ . The instrument has a total mass of 196 kg. Near-infrared (NIR) spectroscopy at higher spectral resolution of up to  $R = \lambda/\Delta\lambda = 50,000 - 100,000$ , as required by science cases like, e.g. exoplanet atmospheres, stellar astrophysics, accretion and outflow of young stellar objects, or chemistry of the interstellar medium, would require a cross-dispersion echelle spectrograph that would be hugely more demanding in mass and volume, as can be appreciated from a ground-based example such as the CRIRES instrument at the ESO Very Large Telescope [2]. It is therefore worthwhile to study the achievable performance in terms of spectral resolution, spectral range, and throughput of a NIR integrated photonic spectrograph towards a future replacement of conventional optics in space applications. This paper is a first in a series where we begin our study with custom-designed AWGs that were derived from canonical layouts known from the literature, in what follows Gen-I. Paper II will address Gen-II AWGs with three-stigmatic-point designs, and Paper III is going to discuss echelle gratings, for comparison with Gen-I and Gen-II AWGs.

Arrayed waveguide gratings (AWGs) have already been studied for their properties as primary dispersive elements in integrated photonic spectrographs, especially for astronomy [3–6]. Descriptions of the fundamentals of AWGs and their modelling and design are found in the literature [7–12], and the principal structure of a typical AWG device is shown in Figure 1(a). Figure 1(b) illustrates the propagation of light through the star coupler segments of the AWG, simulated using the beam propagation method (BPM), which was applied in the development of the building blocks for the AWG designs presented in this paper.

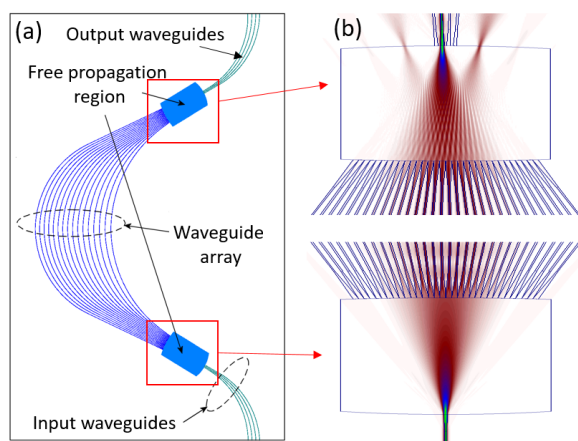


Fig. 1. (a) Structure of an AWG device. (b) BPM simulation of light propagation through the input/output star coupler regions.

While commercially available AWGs are well-optimized for dense wavelength division multiplexing (DWDM), they are not suited for use in high-resolution spectroscopy. The practical implementation of high resolution AWGs poses significant challenges regarding fabrication tolerances and the resulting impact on the device performance. This work presents an experimental study of custom-designed AWGs on a 2% refractive index contrast silica-on-silicon platform, targeting spectral resolving powers  $R = 15,000 \dots 60,000$  in a region of the near-infrared astronomical H-band covering 1500 nm - 1700 nm.

The combined requirement of high spectral resolution and large wavelength coverage of a few hundred nm calls for operation in high spectral orders, which inevitably narrows the free spectral range (FSR) of the AWG to 10 nm - 20 nm. If the spectrum of the input signal covers more than one FSR, the spectral image on the output facet of the AWG will contain multiple overlapping spectral orders with a wavelength spacing of one FSR between to adjacent orders. A cross-dispersion technique is employed to overcome the FSR limitation by separating the overlapping spectral orders by means of a second dispersive element such as a grating or a prism, which is introduced into the optical path after collimation of the AWG output. The collimated beam is dispersed by the second dispersive element in the direction perpendicular to the dispersion of the AWG, introducing a slow dispersion axis for the vertical separation of the spectral orders. In an optimized system, the ratio of angular dispersions of the AWG and the cross-disperser should equal the total number of spectral orders in the operating wavelength range in order to utilize the detector area most effectively. In our instrument design, we are planning to use an Al-coated ruled grating with 600 grooves/mm and a blaze wavelength of 1600 nm. Figure 2(a) shows the principle of a cross-dispersion-assisted AWG spectrograph. The cross dispersion produces a series of spectra called echellogram, shown in Figure 2(b), whereby each spectrum covers one FSR of the AWG. The example shown in Figure 2(b) assumes one single-input AWG device, and a Teledyne H2RG HgCdTe array with  $2048 \times 2048$  18  $\mu\text{m}$  pixels as the detector,

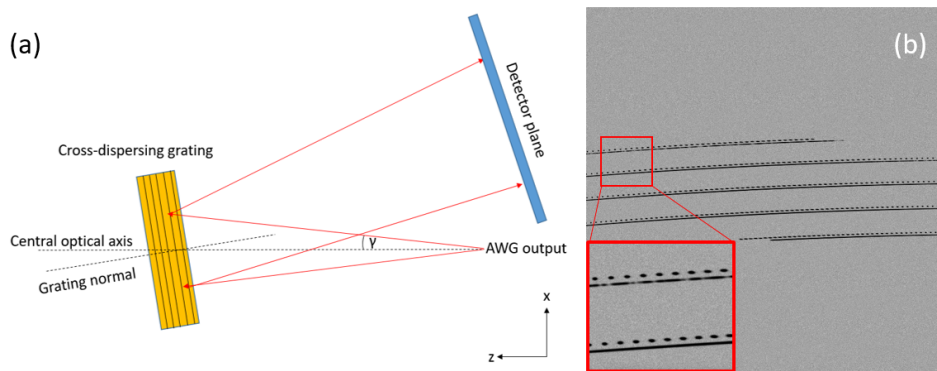


Fig. 2. (a) Principal sketch of an AWG spectrograph utilizing cross-dispersion (AWG chip not shown), the detailed opto-mechanical design is presented in [13]. (b) Simulated echellogram as imaged by the detector prior to data reduction. Example showing a continuous signal under atmospheric absorption accompanied by a discrete calibration spectrum generated by a frequency comb.

leaving most of the detector area unused. A more efficient configuration can be achieved by using multiple inputs on a single AWG [14] or by combining multiple single-input AWG devices into a multi-fibre stack [15] or a possible combination of both.

The fabrication of functional high-resolution AWGs poses significant challenges in terms of fabrication accuracy. High-resolution AWGs with hundreds of waveguides and optical propagation lengths on the order of cm are very susceptible to phase error induced image degradation, leading to fabrication tolerance limited performance [16, 17]. In earlier publications, we have studied the potential and technical limitations of silica-platform AWG, with a focus on the effects of fabrication tolerance related phase errors and the necessity of AWG post-processing by means of UV trimming [16, 18]. In this work, we experimentally study several different AWG designs of varying resolving power on a silica-on-silicon platform. We show AWG designs of varying foot-print, study the spectral transmission characteristics of fabricated AWG chips, and compare the results to theoretical expectations with the goal to determine the practical feasibility of high-resolution AWGs for spectroscopy.

## 2. Design of the basic waveguide structure

Arrayed waveguide gratings of the Rowland-family are by far the best known type of AWGs due to its origin in the telecommunication industry, which optimized the Rowland AWG design in accordance with its needs. In the first iteration of our custom AWG designs, we have implemented the well-known Rowland geometry in various arrangements of waveguide arrays and star couplers, waveguide array sizes between 360 and 722 waveguides, and theoretical spectral resolutions ranging from 0.1 nm to 0.026 nm. The designs were aimed at fabrication on an atmospheric pressure chemical vapour deposition (APCVD) Silica-on-Silicon material platform with a core refractive index contrast of 2%, which was set by the process used by the foundry. Silica-on-silicon technology was selected as a well-developed and reliable platform in order to minimize the risk of failure, as only one fabrication run could be carried out. Furthermore, a low refractive index contrast of 2% allows for very efficient fibre-chip coupling using single-mode high-NA fibres. Certain newer technologies, such as silicon nitride TriPleX [19], are comparable with silica technology in terms of propagation loss. However, due to the large aspect ratio of the SiN core, strong geometrical birefringence is to be expected, which is not desirable for our application.

The building blocks of the AWG structure, such as buried channel waveguides, circular

waveguide bends, taper waveguides and slab waveguides were independently modelled and simulated using a full-vectorial 3D BPM method, implemented in the commercial software RSoft BeamPROP. Simulation of the AWG devices as a whole was carried out using custom-written code based on a scalar diffraction model which relies on the BPM simulation results of the individual building blocks to calculate diffraction images at the output end of the AWG star coupler.

The starting point of Arrayed Waveguide Grating modelling is the definition of material parameters of the waveguide structure. The most basic property of an optical waveguide is the material refractive index of the waveguide core and surrounding cladding and the refractive index contrast between cladding and core. These quantities are determined by the material platform and fabrication process and ultimately dictate the waveguide geometry, namely the single-mode cut-off cross-section of the core, as well as the maximum possible waveguide curvature due to bend waveguide mode leakage. Numerical modelling of basic building blocks of an AWG device can be carried out, once the fundamental waveguide structure of the AWG design has been worked out.

### 2.1. Design of the waveguide core

The target material platform of the AWG design is Ge-doped silica-on-silicon with a low refractive index contrast of 2%. The waveguide design is implemented as a buried-channel waveguide type consisting of three  $SiO_2$  layers on top of a Si-substrate. A symmetric aspect ratio of 1:1 is chosen for the waveguide core in order to minimize waveguide mode birefringence. In the first design step, the single-mode cross-section of the waveguide core must be determined for the shortest wavelength of the working range of the AWG device by numerical simulation. The single mode condition must be satisfied in the entire wavelength range of operation, therefore the single-mode cut-off core cross-section must be determined at 1500 nm. The low-contrast,

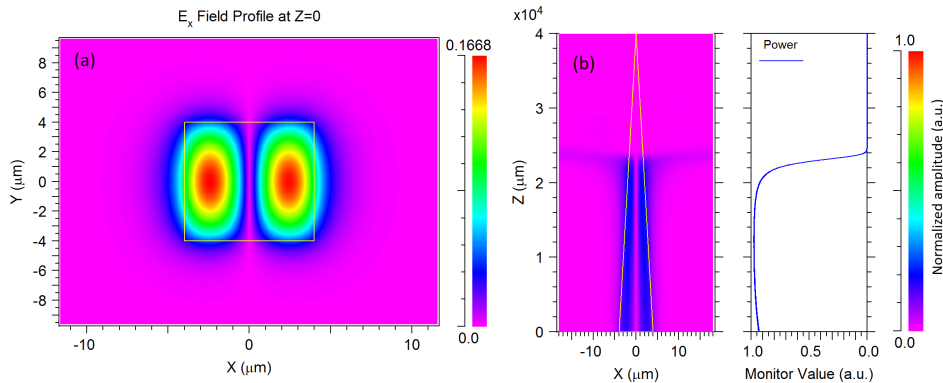


Fig. 3. (a)  $TEM_{10}$  mode of the symmetric  $8 \mu\text{m} \times 8 \mu\text{m}$  rectangular channel waveguide core at 1500 nm. (b) Propagation of the  $TEM_{10}$  mode through a 40 mm long square-profile linear taper waveguide. Power monitor indicates loss of confinement.

square cross-section channel waveguide was modelled as a rectangular core region of width  $w$  and height  $h = w$  with a refractive index  $n_{\text{core}} = 1.4738$  embedded in a cladding with a refractive index  $n_{\text{clad}} = 1.444$  at 1550 nm (silica). A mesh resolution of 100 nm and propagation step size of  $2 \mu\text{m}$  was used. The 3D-waveguide was simulated in full-vectorial mode. Starting from a multi-mode cross section  $w \times h$  of  $8 \mu\text{m} \times 8 \mu\text{m}$ , the first higher propagating mode was calculated using a BPM mode solver with a two-pass correlation method, described in [20]. The single mode cut-off core cross-section was determined by simulated adiabatic deconfinement of

the  $TEM_{01}$  mode, whereby the previously calculated mode was used as the launch field, which was propagated through a long, inversely tapered waveguide. The waveguide core parameter  $w$  was varied along a linear gradient between  $8\ \mu\text{m}$  at  $z = 0\ \mu\text{m}$  and  $0\ \mu\text{m}$  at  $z = L$ . The slow reduction of the waveguide core cross-section along the propagation axis gradually weakens the confinement of the  $TEM_{01}$  mode, until the cross-section reaches a critical value at which the waveguide supports only the fundamental propagating mode. The waveguide construction used in the simulation is shown in Figure 3. To ensure adiabatic conditions during the simulated

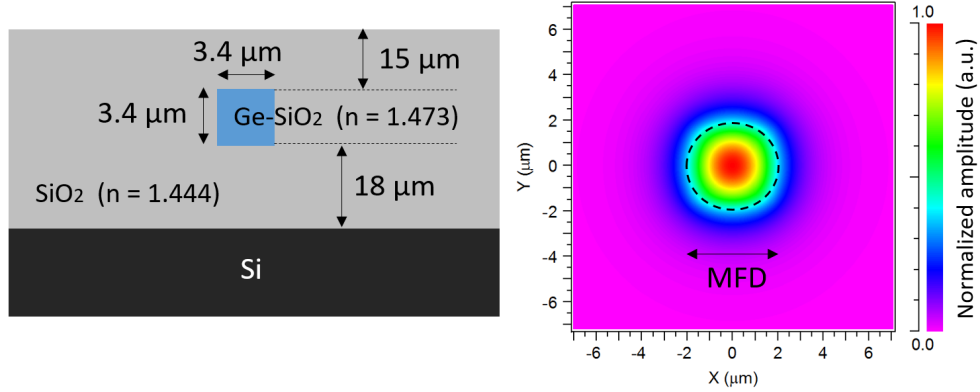


Fig. 4. Left: lithographic structure of the waveguide core design (end-on view, not to scale). Right: propagating fundamental waveguide mode of a  $3.4\ \mu\text{m} \times 3.4\ \mu\text{m}$  waveguide core at 1500 nm

mode propagation, a taper length of 40 mm, correspondingly tapering angle of  $10^{-4}$  rad was chosen, satisfying the adiabaticity condition for the local angle of the taper wall with the central axis of the waveguide  $\theta(z) < \lambda_0 / (2w(z)n_{\text{eff}})$  [21], which, in our case, suggests a tapering angle  $\leq 6 \times 10^{-2}$  rad at  $z = 0$ . The relevant quantity to be determined is the waveguide core dimension  $w_0$  at which the  $TEM_{10}$  mode of the rectangular waveguide loses confinement and dissipates. Due to the symmetry of the waveguide, the same behaviour is expected for the  $TEM_{01}$  mode. In this work, the critical waveguide core dimension was determined by observing the propagation of the mode through the tapered waveguide at 1500 nm. The confinement of the mode field in the waveguide core region during propagation was monitored by integrating the power density in a  $8\ \mu\text{m} \times 8\ \mu\text{m}$  rectangle containing the waveguide core at the centre. Figure 3 shows the launch mode field used for excitation of the waveguide and the x-z slice of the field propagation through the waveguide. Loss of mode confinement is indicated by a sudden drop of partial power in the region of measurement around the waveguide core at a critical z-value, defined by the half-maximum location of the monitor curve, beyond which point the  $TEM_{10}$  mode cannot propagate. In the given case of  $\Delta = 0.02$  and the aforementioned simulation setup, loss of confinement was observed at  $z = 2.3 \times 10^4\ \mu\text{m}$ , or  $w = 3.4\ \mu\text{m}$ . Therefore, a waveguide core layer thickness  $t = 3.4\ \mu\text{m}$  and base waveguide width  $w = 3.4\ \mu\text{m}$  were selected for the AWG designs presented in this work. The dissipation of higher modes was confirmed by simulations of propagation through a 10 mm long waveguide. The choice of the largest core cross-section that guarantees single-mode operation at the shortest wavelength results in optimal confinement of the propagating mode, which in turn results in less evanescent field interaction between nearest neighbour waveguides, as well as lower bend leakage and thus smaller bend radii, contributing to a higher waveguide integration density. The method of adiabatic deconfinement proved to be more reliable than correlation-method BPM mode solving. In cases close to the cut-off condition, where multimode propagation was still observed in simulation runs, the mode solver failed to find

the higher mode, falsely indicating single mode behaviour. The adiabatic inverse tapering method guaranteed the single-mode condition in the simulation and provided a faster way to determine the critical core cross-section, requiring only one propagation run instead of multiple runs needed with a mode solving approach. The schematic cross-section of the waveguide structure and the fundamental propagating waveguide mode are shown in Figure 4.

## 2.2. Minimal radius of a circular bend

In commonly used AWG designs, the waveguide array contains curved segments of either fixed or variable curvature. Optimization of the AWG device foot-print affects the radii of curvature in the waveguide array and therefore requires prior knowledge of the minimal acceptable waveguide bend radius. In order to study bend leakage in a circular bend waveguide, we have numerically simulated mode propagation through a 10 mm long circular bend using BPM. A series of simulations was performed to study mode propagation through bends of varying radii in a wavelength range between 1500 nm and 1700 nm. Mode leakage was measured by monitoring the exponential decay of mode power in the waveguide core along the propagation direction. Finally, the bend losses were obtained by linear fitting of the logarithm of the power monitor evolution curves. Figure 5 shows the simulated bend losses in a range of bend radii  $R_b$  between

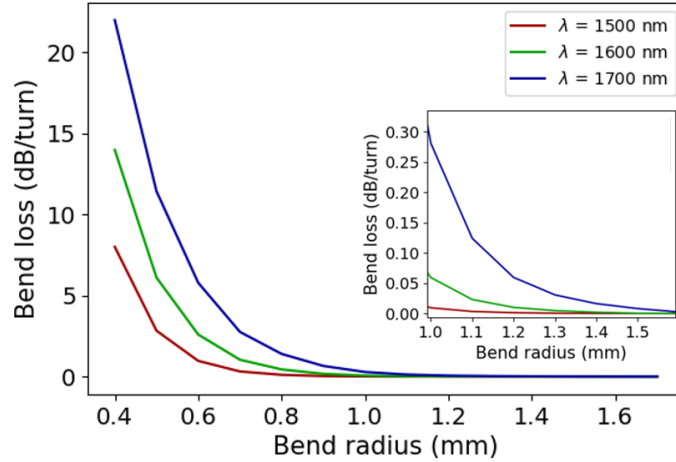


Fig. 5. Simulated bend loss for a  $3.4 \mu\text{m} \times 3.4 \mu\text{m}$  square-profile waveguide core of varying bend radius at three wavelengths in the range 1500 nm - 1700 nm.

0.4 mm and 1.7 mm. The results show an increase of bend losses with increasing wavelength for all bend radii in the simulated range. Waveguide bends with  $R_b < 0.7$  mm exhibit prohibitively high leakage of  $> 1$  dB per  $360^\circ$  turn at 1500 nm and  $> 3$  dB/turn at 1700 nm. The losses rapidly decrease with increasing bend radius and fall below  $10^{-2}$  dB/turn for  $R_b > 1.4$  mm at 1700 nm. In this work, a minimum bend radius of 1.5 mm was chosen in order to reduce bend leakage loss to a negligible level between  $1.95 \times 10^{-6}$  dB/turn at 1500 nm and  $7.98 \times 10^{-3}$  dB/turn at 1700 nm.

## 3. Definition of spectral requirements

The AWG designs constructed in this work are aimed at applications as a core dispersive element in a compact astronomical spectrograph operating in the astronomical near-infrared H-band window of atmospheric transparency. The goal of the design is to achieve high throughput ( $< 3$  dB insertion loss) as well as a high spectral resolving power. The comparatively small

length of the free propagation region on the order of 1 cm limits the width of the wavelength-dispersed diffraction image to a few hundreds of  $\mu\text{m}$  to a few mm. The width of the constructive interference peak on the image plane is fixed by the mode profile of the input waveguide and the maximum number of separable spectral lines is severely restricted by the narrow width of the wavelength-dispersed image. Therefore, in order to achieve a high spectral resolution, one has to limit the free spectral range of the AWG to a few tens of nm by defining a sufficiently large waveguide array path length increment corresponding to high diffraction orders. In our AWG designs, diffraction orders of up to  $m = 94$  were used. In order to study the feasibility of increasingly higher spectral resolutions, target resolving powers of 15,000, 30,000 and 60,000 (corresponding to spectral resolutions of 0.1 nm, 0.052 nm and 0.026 nm, respectively) were defined for low-resolution, mid-resolution and high-resolution designs. Target *FSRs* of 16 nm, 23 nm, 32 nm and 48 nm were defined to study the performance of waveguide arrays in a range of varying spectral bandwidths.

#### 4. Design of the array-FPR interface

The starting point of the AWG construction in this work is the design of the array-FPR interface and the fan-out section of the AWG, as it determines the minimum required distance between waveguides at the FPR interface, and hence the waveguide width as well as the number of waveguides in the array.

##### 4.1. Minimum waveguide separation distance

The integration density of an AWG device partly depends on the maximum amount of acceptable inter-waveguide crosstalk by evanescent field coupling. Depending on the refractive index contrast of the material, a minimum distance between waveguides must be observed to prevent degradation of the point spread function due to excessive cross-coupling. The starting point of the AWG design, after definition of the bulk material properties, is the determination of the minimum nearest-neighbour waveguide separation at the interface between the waveguide array and FPR slab. In this work, this procedure was performed by numerical simulation of light propagation through the fan-out segment of the array-FPR interface using 3D BPM. For this purpose, a simplified model of the fan-out was created in the RSoft CAD utility, shown in Figure 6 (left). Evanescent coupling was studied by selectively exciting a single waveguide and observing the transmitted power via a power monitor located inside the waveguide cores. The FPR radius was varied between 4 mm and 20 mm and the distance between adjacent waveguides at the FPR interface (grating pitch)  $d$  was varied between 8  $\mu\text{m}$  and 15  $\mu\text{m}$  in a series of simulations at  $\lambda = 1700$  nm, where evanescent field coupling is expected to be strongest in the wavelength range of the AWG. The total amount of power transferred to the neighbouring waveguides was defined as  $1 - P$ , where  $P$  is the normalized mode power remaining in the initially excited waveguide after propagation through the fan-out. Figure 6 (right) shows the simulated cross-talk between the waveguides as  $10 \log(1 - P)$  over the grating pitch for a range of grating radii between  $R = 4$  mm and  $R = 20$  mm. Increasing cross-talk can be observed for smaller values of the grating pitch and larger grating radii, which is to be expected since both parameters reduce the fan-out angle of the waveguides and thereby prolongs evanescent interaction, causing more power to be transferred between nearest neighbours. The cross-talk in our simulation varies from nearly 0 dB (complete power transfer to nearest neighbours) at  $d = 8 \mu\text{m}$  and  $R = 20$  mm to less than -40 dB (negligible coupling) at  $d = 14 \mu\text{m}$  and  $R = 4$  mm. In this work, we use  $d = 10.57 \mu\text{m}$  as a compromise between waveguide array cross-talk and device foot-print. In our expected range of FPR radii used for the AWG designs, the simulation results predict a cross-talk level of -16 dB...-30 dB in the worst case  $\lambda = 1700$  nm.

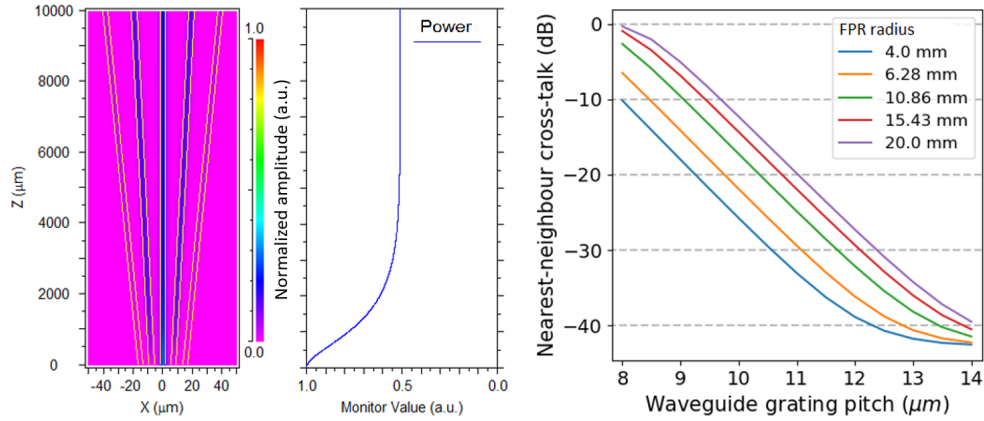


Fig. 6. Left: Simplified model of the fan-out region showing propagation of light through a single waveguide at the centre. The power monitor curve shows the transfer of power from the active waveguide to adjacent waveguides. Right: Nearest neighbour cross-talk caused by evanescent field coupling for varying values of the FPR radius, or correspondingly varying focal lengths. Simulated at  $\lambda = 1700$  nm.

#### 4.2. Tapering of the array-FPR interface

Adiabatic mode size conversion plays an important role in integrated photonic circuits. Its primary purpose is the optimization of transmission efficiency between different components of the circuit, such as channel waveguides and slab waveguides. Mode size conversion is typically achieved by introducing a longitudinal waveguide core width gradient between an initial core width and the desired final core width. Such an element is called a waveguide taper. As an integral part of AWGs, tapers serve to create a smooth transition between the plurality of narrow-core array waveguides and the free propagation region in order to minimize coupling loss by mode matching of the waveguide array and the FPR slab waveguide. Since the minimum acceptable waveguide separation distance is significantly larger than the channel waveguide core width, tapering of the array-FPR interface is essential to ensure a high transition efficiency. Various types of taper geometries exist, with the most common being the linear horn taper, which is implemented in the AWG designs in this work. A sufficient taper length must be observed to ensure quasi-adiabatic mode size conversion, avoiding higher order mode excitation in the multi-mode segment of the taper. The light coupling behaviour of the tapered waveguide array was studied numerically using 3D BPM on a simple model of the structure consisting of a few waveguides in an arrangement that resembles the real arrangement of waveguides in an AWG device. This approach allows to accurately simulate the isolated coupling efficiency of the array-FPR interface while conserving a substantial amount of computational resources. The BPM simulations were performed on a laterally truncated segment of the array-FPR interface, as shown in Figure 7. The array of tapers was excited with a laterally uniform optical field, which was defined as  $E(x, y) = \psi(y)$ , where  $\psi(y)$  is the slab waveguide mode function. In order to minimize boundary artifacts, all measurements were taken on the centremost waveguide of the array. The propagation was simulated at various wavelengths between 1500 nm and 1800 nm. Coupling efficiency was quantified by a mode power monitor situated in the waveguide of interest. The waveguides were arranged equidistantly with a period of  $10.57 \mu\text{m}$ . A gap of  $1.5 \mu\text{m}$  between the edges of the tapers was set in accordance with the safe lower limit of the lithographic process resolution, called minimum feature size, suggested by the integrated photonics foundry which implemented the designs into working prototypes. The array of taper waveguides was excited with a uniform slab mode which was normalized to unit power. Since the simulation region



contains six waveguides, each waveguide in the array received one sixth of the total transmitted power. The efficiency of the interface was calculated as the ratio of the total transmitted power and the input power. The simulation results for TE and TM-polarized input are shown in Figure 7. The left side of the figure shows the simulation setup after one propagation run. The field

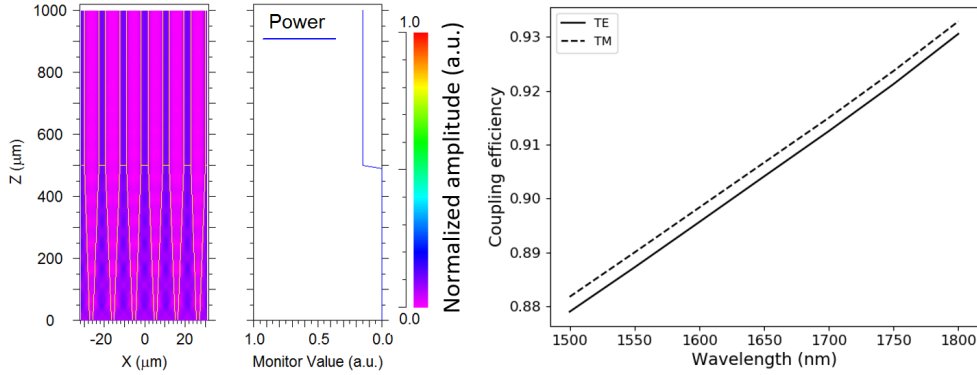


Fig. 7. Left: Simulation setup containing five waveguides. Monochromatic continuous-wave field distribution is colour-coded. The pathway monitor shows the normalized power received by the centremost waveguide relative to the launch power. The taper segments have a length of  $500\ \mu\text{m}$  and a base width of  $9.07\ \mu\text{m}$ . Right: Simulated coupling efficiency of the array-FPR interface for TE and TM-polarized input in the range  $1500\ \text{nm} - 1800\ \text{nm}$ .

amplitude of a monochromatic continuous-wave signal in the simulation region is colour coded in the normalized range  $0 - 1$ . The power monitor value is recorded after propagation through the taper. A wavelength-dependent coupling efficiency varying between  $0.88$  at  $1500\ \text{nm}$  and  $0.93$  at  $1800\ \text{nm}$  is observed for TE-polarized input. The coupling efficiency is marginally higher for the TM polarization. A study of taper efficiency in an earlier AWG design on a  $\Delta = 0.015$  silica-on-silicon platform was presented in [18]. In this study, a  $1\ \text{mm}$  long linear taper of  $14\ \mu\text{m}$  base width was found to exhibit a simulated coupling loss of  $0.31\ \text{dB}$  at  $1500\ \text{nm}$ . The coupling loss was reduced to  $0.088\ \text{dB}$  by introducing a novel discontinuous taper structure which takes advantage of multi-mode interference. The MMI taper is one of the possible loss reduction mechanisms under consideration for future iterations of the AWG designs.

#### 4.3. Aperture of the waveguide grating

In order to achieve a high transmission efficiency as well as minimize truncation sidelobes of the diffraction image, it is important to design a waveguide grating with a sufficiently large aperture, i.e. angular width of the array-FPR interface, which covers most of the input beam cross-section. On the other hand, the aperture size should be as small as possible in order to minimize the foot-print and number of waveguides of the AWG structure, reducing the potential for phase errors. The calculation of the waveguide array aperture size is based on the known near-field distribution of the input waveguide mode, from which an angular far-field distribution at the FPR-array junction is derived. In this work, we have designed the width of the waveguide grating to cover  $99\%$  of the incoming beam power, corresponding to a negligible truncation loss  $0.044\ \text{dB}$ . The associated aperture angle covering  $99\%$  of the beam power is  $0.434\ \text{rad}$ . The left side of Figure 8 shows the angular intensity profile of the input beam far field. The dashed lines mark the boundaries of the region containing  $99\%$  of the input beam power. The right side of the figure shows the normalized input intensity distribution (red curve) and the normalized output intensity distribution (blue curve). The truncation of the beam to  $0.434\ \text{rad}$  induces sidelobes of  $-28\ \text{dB}$

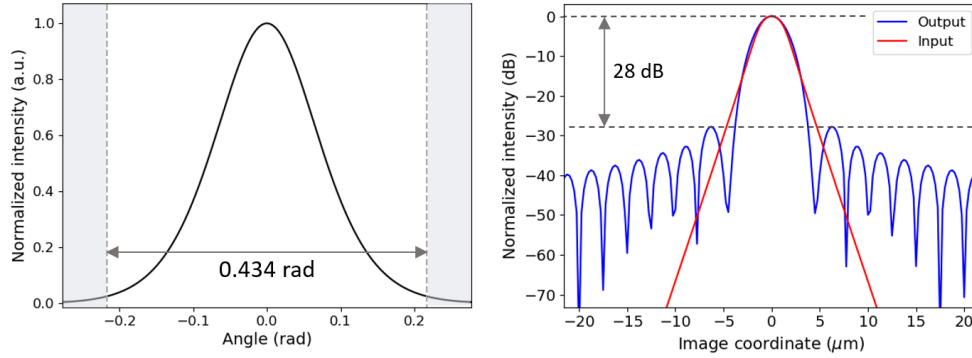


Fig. 8. Left: Normalized intensity distribution of the input waveguide far field with truncation boundaries indicated by dashed lines. Right: Reconstructed near field intensity profile of the truncated far field distribution (blue), input field intensity profile (red).

peak intensity in the output diffraction image.

The calculation of the minimum required focal length from the minimum waveguide separation distance, angular grating aperture and resolution requirement is described in the next section.

## 5. Geometrical construction of the AWG layout

The structure of the AWG can be arranged in various ways. The choice of an appropriate waveguide layout mainly depends on the grating order and thus the geometrical path length increment of the waveguides. AWG geometries can be roughly distinguished into three types: low-order, medium-order and high-order AWG devices, each requiring a specific arrangement of waveguides. Low-order AWGs with small path length increments are suitable for wide-band, low-resolution wavelength demultiplexing. The waveguide array of this AWG type is arranged in an S-geometry, which allows for very small path length increments while maintaining the required minimum distance between waveguides. The S-type is suitable for large free spectral ranges above 50 nm. Medium-order AWGs are typically realized in the conventional horse-shoe geometry. This type of AWGs has been widely used for DWDM applications in optical telecommunications, as they offer a good balance between spectral resolution and spectral bandwidth with free spectral ranges between 30 nm and 50 nm in this particular application case. High-order AWGs with a large path length increment can achieve high spectral resolutions at the cost of reduced free spectral range. This type of waveguide array requires sufficient space for path length accumulation. Therefore, a folded design is chosen which allows the waveguides to "balloon" outwards. The free spectral range of this AWG type is typically < 20 nm. In this work, horse-shoe-type and folded-type AWGs are selected and implemented for a wide FSR at low-medium spectral resolutions and a narrow FSR at low-high spectral resolutions, respectively.

This work presents five different AWG devices designed to operate in spectral orders between  $m = 31$  and  $m = 94$ . Two AWG designs were implemented as folded-type AWGs, from here on denoted as type A and type B. Three designs were implemented as horse-shoe type AWGs, referred to as type C, D and E. Designs of type A and B operate in the same spectral order  $m = 94$ , which corresponds to a FSR of 16 nm. Design A is the largest AWG in the group, having a focal length of 18 mm and a waveguide array size of 722. Design B is directly derived from design A through down-scaling by a factor of 0.5. Since the input waveguide properties are identical in all six AWG variants, they all share the same angular grating aperture of 24.4 degrees. The AWG layouts were implemented with careful observation of geometrical consistence, avoiding

any discontinuities of optical paths, maintaining the minimum waveguide separation distance, minimum lithographic feature size, as well as a minimum waveguide bend radius to minimize bend leakage. All designs were equipped with 30 output waveguides evenly distributed over the output facet of the slab waveguide for characterization purposes.

### 5.1. Calculation of FPR length based on resolution criterion

Given a fixed size of the input waveguide core, the spectral resolution of the AWG is determined by the waveguide array path length increment, the number of waveguides, the grating pitch and the focal length, which is identical to the length of the FPR slab waveguide. Requiring a certain spectral resolution  $\Delta\lambda$ , one must ensure that overlapping peaks corresponding to  $\lambda$  and  $\lambda + \Delta\lambda$  can be identified as separate features in the spectral image. In this work, we obtain lower estimates for the required focal length using the full-width-half-maximum (FWHM) resolution criterion, assuming two spectral lines separated by approximately one FWHM are just barely resolvable as separate intensity maxima. The necessary condition for the focal length is derived from the AWG grating equation [22], yielding a change of the diffraction angle  $\theta$  at  $\lambda_0$  as

$$\Delta\theta \approx \left. \frac{d\theta}{d\lambda} \right|_{\lambda_0} \Delta\lambda = \frac{\lambda_0^2}{R \cdot FSR \cdot d \cdot n_s} \quad (1)$$

where  $n_s$  is the slab waveguide effective index,  $d$  is the grating pitch and  $\Delta\lambda \ll FSR$ . Requiring  $L_f \Delta\theta \geq w_{1/2}$ , we obtain the condition for the focal length  $L_f$  for any given combination of spectral resolving power  $R$  and  $FSR$  as

$$L_f \geq \frac{R \cdot FSR \cdot n_s \cdot d}{\lambda_0^2} w_{1/2}, \quad (2)$$

where  $w_{1/2}$  is the *FWHM* of the squared input waveguide mode field. The input waveguide with

Table 1. Minimum required focal length in mm as a function of free spectral range and resolving power.

R	FSR (nm)			
	16	23	32	48
15,000	4.055	5.83	8.11	12.165
30,000	8.11	11.66	16.22	24.33
60,000	16.22	23.32	32.44	48.66

a 2% refractive index contrast core measuring  $3.4 \mu\text{m} \times 3.4 \mu\text{m}$  produces a mode field with an intensity *FWHM* of  $2.62 \mu\text{m}$  and is used in all AWG designs presented in this work. The slab waveguide effective index at 1550 nm is calculated as  $n_s = 1.4661$ . Given  $d = 10.57 \mu\text{m}$  and  $\lambda_0 = 1550 \text{ nm}$ , we obtain the minimum required focal length as a function of  $FSR$  and  $R$  only, presented in Table 1.

### 5.2. Construction of the waveguide array

As the central element of the AWG device, the waveguide array serves as a multipath optical delay line consisting of several hundreds of single-mode waveguides of length  $L_j = L_{j-1} + \Delta L$ , where  $j$  is the waveguide number and  $\Delta L = m\lambda_0/n_{\text{eff}}$  is a fixed path length difference between nearest neighbour paths, defined by the integer grating order  $m$ , the central wavelength  $\lambda_0$  and the waveguide effective index  $n_{\text{eff}}$ . Since the spectral requirements imposed on the designs in section 3 define  $\lambda_0$  and the free spectral range as the design parameters, the appropriate grating

order  $m$  must be determined for each design. The free spectral range of the AWG is given by  $FSR = n_{\text{eff}}n_g\lambda_0/m$ , where  $n_g$  is the waveguide group index. Hence, the grating order is calculated as

$$m = \left\lceil \frac{n_{\text{eff}}\lambda_0}{n_g FSR} \right\rceil, \quad (3)$$

where the square brackets on the right hand side indicate rounding to the nearest integer. The values  $n_{\text{eff}}$  and  $n_g$  were obtained from numerical simulations of the array waveguide core as  $n_{\text{eff}} = 1.4586$  and  $n_g = 1.4959$  at  $\lambda_0 = 1550$  nm.

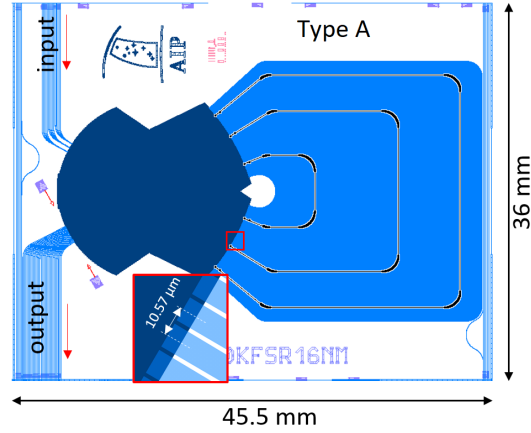


Fig. 9. Lithographic mask layout of the largest AWG design (Type A). Theoretical  $R = 60,000$ . Three selected array waveguides highlighted showing straight and curved waveguide segments.

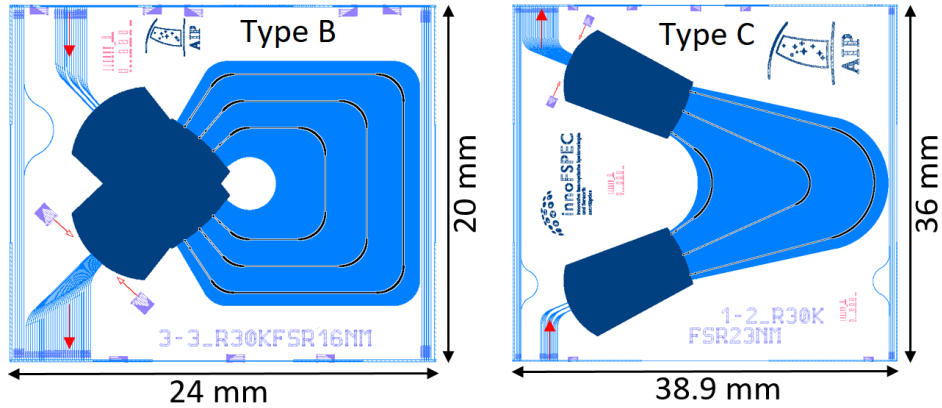


Fig. 10. Lithographic mask layouts of AWGs B and C. Theoretical  $R = 30,000$ . Type B is conceptually similar to type A, containing five straight segments and four curved segments in the waveguide array. Type C is a traditional design consisting of two straight segments and one curved segment.

The required grating order values were calculated as  $m = 94$ ,  $m = 66$ ,  $m = 47$  and  $m = 31$ , corresponding to free spectral ranges of 16.08 nm, 22.9 nm, 32.2 nm and 48.8 nm, respectively. Note that, for any given central wavelength, the FSR is restricted to a discrete set of values which corresponds to the integer values of  $m$ . Therefore, the actual FSR deviates slightly from the

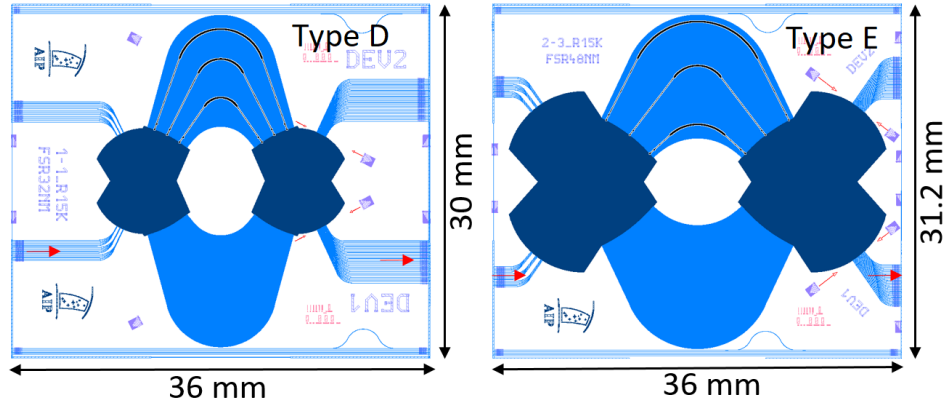


Fig. 11. Lithographic mask layouts of AWGs D and E. Theoretical  $R=15,000$ . Both AWGs are conceptually similar to type C.

Table 2. Specifications of AWG designs A-E.

Type	FSR (nm)	$\Delta\lambda$ (nm)	R	$L_f$ (mm)	$N_{wg}$	$\Delta L$ ( $\mu\text{m}$ )	Footprint ( $\text{cm}^2$ )
A	16.08	0.026	60,000	18	722	99.89	16.38
B	16.08	0.052	30,000	9	360	99.89	4.8
C	22.9	0.052	30,000	12.728	512	70.1	14.0
D	32.2	0.1	15,000	9	362	49.9	10.8
E	48.8	0.1	15,000	13.5	543	32.9	11.23

design values used to calculate  $m$ . With the known grating order values, the geometrical path length increments  $\Delta L$  of the AWG designs was calculated accordingly as 99.89  $\mu\text{m}$ , 70.1  $\mu\text{m}$ , 49.9  $\mu\text{m}$  and 32.9  $\mu\text{m}$ . Appropriate waveguide array geometries were selected for each case in order to minimize the foot-print of the designs as well as the length of the optical paths. The waveguide arrays with the largest path length increment of 99.89  $\mu\text{m}$  were implemented in a folded arrangement consisting of nine segments of alternating straight and curved waveguide sections with a constant curvature radius of 1.5 mm, as shown in Figure 9. The distance between nearest-neighbour waveguides in the central bulk of the array was required to be  $\geq 15 \mu\text{m}$  in order to prevent evanescent field coupling. The folded geometry was used for AWG designs of type A and type B, while the traditional horseshoe geometry was used for types C, D and E. The largest design of type A contains 722 waveguides with lengths between 7 mm and 79 mm. The AWG design of type B, shown on the left of Figure 10, is a down-scaled version of type A, containing 360 waveguides. AWG designs with the horseshoe type are shown in Figure 10 (right) and Figure 11. The array waveguides of these designs consist of two straight sections and a central curved section of variable radius  $\geq 1.5$  mm. In design C, the bend radius varies from 1.654 mm to 6.635 mm. The variation in design D is between 1.586 mm and 4.803 mm and design E uses bends with radii between 2.025 mm and 6.570 mm. The smallest radii are found roughly in the first third of the waveguide array, counting from the shortest waveguide. Despite an equal resolving power, the required number of waveguides is larger in type C as compared to type B due to the larger FSR of 23 nm. The nearest-neighbour path length increment is 70.1  $\mu\text{m}$  in the type C design. The foot-prints of the final designs range from 4.8  $\text{cm}^2$  (type B)

to 16.38 cm<sup>2</sup> (type A). Each design contains arrays of input and output waveguides, which do not use tapering in order to minimize the spot size of the input near field and thus maximize the achievable resolution. An array of 31 output waveguides distributed equidistantly across the spectral image region of the output FPR facet was integrated in each design for testing purposes. The design specifications of all five AWG types are summarized in Table 2.

## 6. Numerical simulation of the AWG designs

We have numerically studied the spectral properties of the AWG designs using a segmented simulation approach which employs the beam propagation method in combination with a scalar method based on Fraunhofer diffraction. In the first stage, the optical properties of fundamental AWG building blocks were simulated using 3D-BPM. Specifically, mode profiles of the input waveguides, array waveguides and slab waveguides, as well as their wavelength-dependent effective indices were obtained for the wavelength range of operation. The numerical model included the wavelength-dependent refractive index of the *SiO*<sub>2</sub> cladding from the dielectric material library of the RSoft suite, while the refractive index of the core was calculated from the refractive index of the cladding assuming a fixed contrast of 0.02. The mode profiles of the input waveguides and array waveguides were further processed to obtain their respective far field functions. The pre-calculated far field and effective index data was then used to set up the scalar diffraction model. In the second stage, the wavelength-dependent transmission from input waveguides  $j$  to output waveguide  $k$  was calculated according to [10, 16]

$$T_{jk}(\lambda) = \left| \sum_{l=1}^N c_{jk}(l) \exp(-i\Omega_{jk}(l)) \right|^2 \quad (4a)$$

$$c_{jk}(l) = f(\sigma_{jl})g(\rho_{jl})g(\rho_{kl})h(\sigma_{kl}) \quad (4b)$$

$$\Omega_{jk}(l) = \frac{2\pi}{\lambda} (n_s(r_{jl} + r_{kl}) + n_a((l-1)\Delta L + L_1)), \quad (4c)$$

where  $\Omega_{jk}$  is the accumulated phase after propagation between input  $j$  and output  $k$ ,  $f$ ,  $g$  and  $h$  are angular far field functions of the input waveguides, array waveguides and output waveguides, respectively,  $n_a$  and  $n_s$  are effective indices of the waveguide array and the FPR slab, respectively,  $r_{jl}$  and  $r_{kl}$  are the free propagation distances between the terminus of array waveguide  $l$  and input waveguide  $j$  / output waveguide  $k$ , respectively,  $\sigma_{jl}$  and  $\rho_{jl}$  are propagation angles relative to the axis of the input waveguide  $j$  and array waveguide  $l$ , respectively, and  $\Delta L$  is the waveguide array path length increment. The wavelength transmission spectrum of any given output waveguide is calculated by summation over all contributions from  $N$  array waveguides. Implementation of different AWG designs in this model was accomplished by variation of the path length increment  $\Delta L$  and the  $N$  geometry parameters  $r_{kl}$ .

We have obtained theoretical wavelength channel transmission curves for all five AWG types, calculation results being shown in Figure 12. The transmission includes an insertion loss of 1 dB, obtained from simulations of the array-FPR taper loss and truncation loss in both star couplers, neglecting fibre-chip interfacing loss. Waveguide coupling by evanescent field interaction was not included in this simulation due to the limitations of the AWG model. A full simulation using BPM was not feasible due to the size of the AWG structures. Based on the results in section 4.1, we assumed the coupling and its effects to be negligibly small. The impact of evanescent interaction of array waveguides on the performance of high-resolution AWGs is a subject of future investigation. The three distinct transmission curves in Figure 12 correspond to the different levels of spectral resolving power. The transmission curves are identical for AWGs of equal resolving power, since identical input/output waveguides are used in all designs. The 3 dB-bandwidths of the transmission curves were found to be 0.034 nm for the AWG of type A,

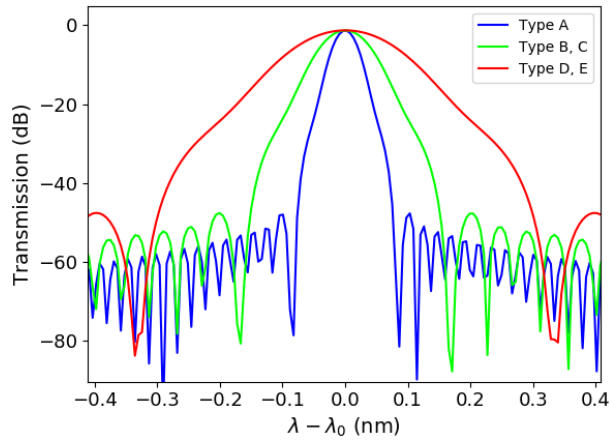


Fig. 12. Power transmission curves of the centremost output channel of AWG types A-E.

0.067 nm for AWGs of types B and C and 0.13 nm for AWGs of types D and E. These values shall be used as reference in the experimental evaluation of the AWG designs.

## 7. Fabrication and characterization

The AWG devices A-E were fabricated by an external foundry (Enablence USA Components, Inc) on a 6-inch Si wafer using UV-photolithography and APCVD technology. A 3.4  $\mu\text{m}$  thick Ge-doped silica core with  $n_c = 1.473$  was deposited on 20  $\mu\text{m}$  of thermal oxide, followed by reactive ion etching (RIE) of the waveguide structure and deposition of a 15  $\mu\text{m}$  thick upper cladding with  $n_{cl} = 1.444$ . Figure 13 shows two fabricated AWG chips of type B (left) and type D (right), implemented in a folded geometry and horse-shoe geometry, respectively.

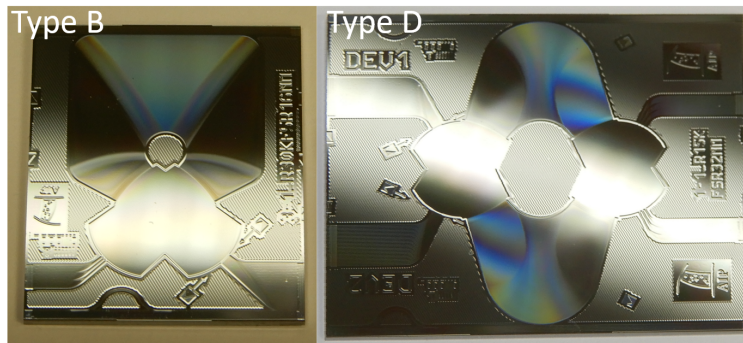


Fig. 13. Fabricated AWG devices of folded-type (left) and horse-shoe-type (right).

A preliminary characterization of the fabricated AWGs was conducted using a T100S-HP CL band tunable laser source (TLS) coupled to a Yokogawa AQ6151 optical wavelength meter (OWM) via a PC running a LabView controller module. Coupling between the TLS and the AWG chips was established via SM1500 fibres with a mode field diameter of 4.2  $\mu\text{m}$ , matching the on-chip waveguide mode  $1/e$  field diameter. The power transmission spectrum was measured at selected output channels to evaluate the channel FWHM and device insertion loss. Measurements were taken relative to a straight reference waveguide located on the same chip.

### 7.1. Wavelength channel transmission

The wavelength transmission spectrum of the fabricated AWGs was measured for selected output waveguides by injection of monochromatic light into the central input waveguide and measurement of the transmitted power on each output waveguide. The wavelength of the TLS was tuned in discrete steps of 0.05 nm. Prior to each set of measurements, reference spectra were recorded for direct fibre-fibre coupling and fibre-waveguide-fibre coupling. Figure 14 shows the transmission spectrum of a 36 mm long straight reference waveguide relative to the TE-polarized TLS background. The measured insertion loss of the straight reference waveguide ranges between 0.16 dB at 1530 nm and 0.28 dB at 1570 nm. The first AWG under test was the largest design of

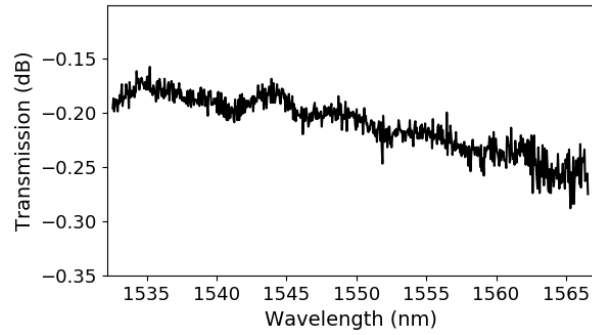


Fig. 14. Transmission spectrum of a 36 mm long reference waveguide relative to TLS background (TE polarization).

type A. This design is very susceptible to aberrations of the waveguide effective index due to refractive index non-uniformities and film thickness, as well as waveguide width variations. The transmission spectra of the centremost output channels are shown in Figure 15. The measured transmission curve is significantly broadened in comparison with the simulated transmission curve, as shown in Figure 15(b). The strong degradation of spectral properties can be attributed to the large average length of the waveguide array of 40 mm, leading to unacceptably large phase errors (see [18]). In a previous work, we have obtained an upper estimate of the effective index variation of  $\delta n_{\text{eff}} = 7.2 \times 10^{-6}$  by measuring the variations of optical lengths in a silica AWG from the same batch as the devices in this work [16]. The estimated spectral resolving power of

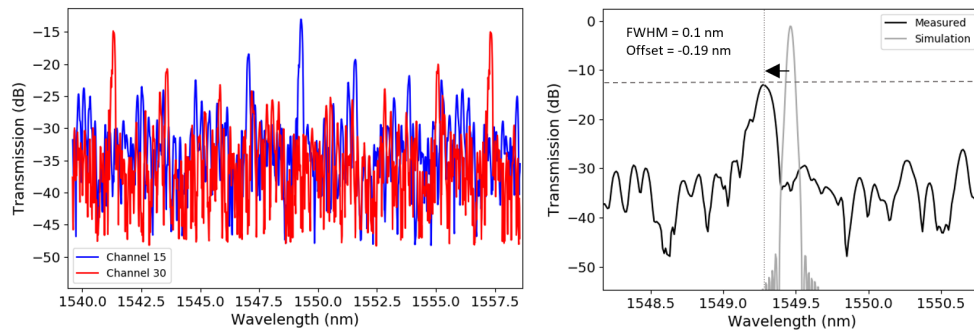


Fig. 15. (a) Type A transmission spectrum of output channels 15 and 30. (b) Main transmission peak in comparison with simulated transmission curve. The measured peak is offset from its theoretical wavelength by  $-0.17$  nm and its 3-dB-bandwidth is 0.1 nm.



the fabricated type A device is  $R > 15,000$  at 1550 nm. The measurement results of the type B AWG are shown in Figure 16. Being a downscaled type A design, the AWG shows similar results, albeit with noticeably lower crosstalk level, as should be expected with a reduction of the average propagation length. Figure 16(a) shows the transmission spectra of three output channels in the central region of the output waveguide interface. The main transmission peak is shown in Figure 16(b). We have estimated a spectral resolving power  $R > 18,900$  at 1550 nm for device B.

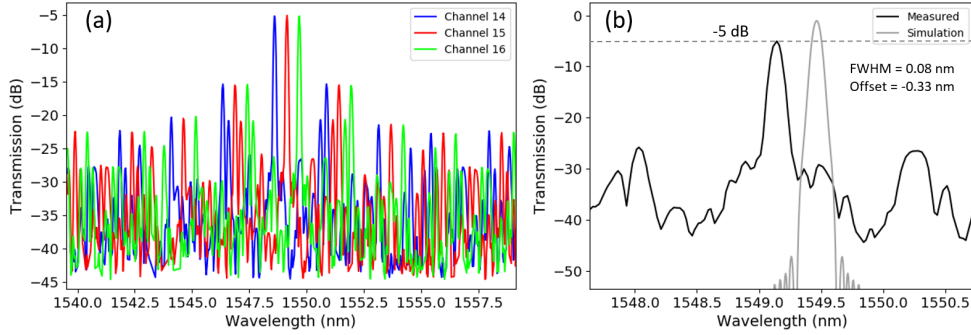


Fig. 16. (a) Type B transmission spectrum of output channels 14-16. (b) Main transmission peak in comparison with simulated transmission curve. The measured peak is offset from its theoretical wavelength by  $-0.33$  nm and its 3-dB-bandwidth is  $0.082$  nm.

The overall comparison with type A results shows a significant improvement of transmission loss and narrowing of the transmission peak bandwidth. Similar measurements were performed on AWGs of types C-E. The measurement results for type C are shown in Figure 17. These results are comparable with type B measurements, with the exception of the larger FSR of type C.

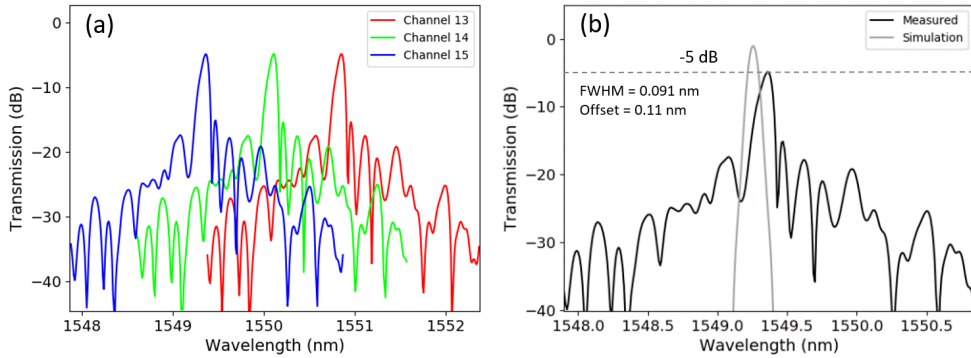


Fig. 17. (a) Type C transmission spectrum of output channels 13-15. (b) Main transmission peak in comparison with simulated transmission curve. The measured peak is offset from its theoretical wavelength by  $0.09$  nm and its 3-dB-bandwidth is  $0.09$  nm.

The transmission measurements on types D and E exhibit similar performance with resolving powers of 11,000 and 10,333, respectively. Measurement results for types D and E are shown in Figures 18 and 19, respectively.

Five fabricated silica AWG designs have been tested for insertion loss and transmission peak FWHM. The measurement results were compared with simulated transmission spectra. For type A, the results have shown a high insertion loss of 13 dB and significant crosstalk level of  $-5$

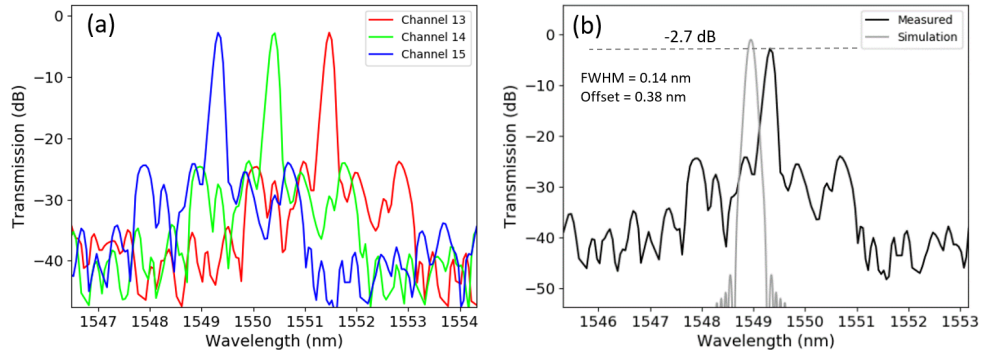


Fig. 18. (a) Type D transmission spectrum of output channels 13-15. (b) Main transmission peak in comparison with simulated transmission curve.

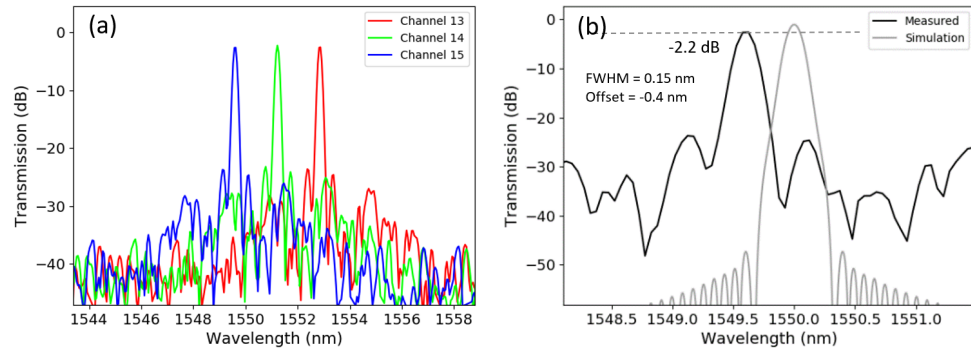


Fig. 19. (a) Type E transmission spectrum of output channels 13-15. (b) Main transmission peak in comparison with simulated transmission curve.

dB, along with a broadening of the channel transmission curve in the largest AWG design of type A. This design is severely impacted by fabrication tolerances, reaching only 25% of its target spectral resolving power. The second group, types B and C, show a similar performance, reaching 57% – 63% of their theoretical resolving power with an insertion loss of 5 dB. Designs of the third group, types D and E, showed the best performance in terms of insertion loss and agreement with target resolution specifications. Insertion loss was lowest for type E at 2.2 dB and slightly higher at 2.7 dB for type D. Transmission peak bandwidth measurements yield 0.14 nm

Table 3. Summarized characterization results of AWG designs A-E.

Type	IL (dB)	Crosstalk (dB)	Bandwidth (nm)	est. $R$	$\lambda_0$ offset (nm)
A	-13	-5	0.1	15,500	-0.19
B	-5	-10	0.082	18,900	-0.33
C	-5	-10	0.09	17,222	0.11
D	-2.7	-21.3	0.14	11,000	0.3
E	-2.2	-22.8	0.15	10,333	-0.4

and 0.15 nm for type D and E, respectively, in fair agreement with the theoretical value of 0.13 nm. In terms of spectral resolving power, types B and C outperform all remaining designs. The measured wavelength offsets of the output channels range from  $-0.4$  nm to  $0.3$  nm, indicating a global variability of the waveguide effective index on the order of  $4 \times 10^{-4}$ . Table 3 summarizes the experimental evaluation of the five AWG designs. It should be noted at this point that the resolving power estimates obtained from channel power transmission measurements are lower than the actual maximum resolving power of the AWGs when the spectrum is imaged directly. This is owed to the fact that power transmission curves are convolutions of the focused beam with the receiver waveguide mode. Deconvolution of the transmission spectrum reveals the focused image and yields a higher resolving power.

## 7.2. Dicing of the output facet

While an array of densely spaced output waveguides can be used for the sampling of the spectrum, the spectral resolution of such a configuration is limited by the integration density of the output waveguides. Applications in high-resolution spectroscopy benefit from direct imaging of the spectrum on a flat, polished end facet of the output FPR. Devices of type C and E were selected for further processing due to the high spectral resolution of type C and the low insertion loss of type E. Device B, while having a higher resolving power than device C, was retained for further study. The procedure consists of cutting the output facet along a straight line intersecting the FPR just below the output waveguides, followed by polishing the facet to optical quality, schematically shown in Figure 20. After dicing and polishing, spectral images can be acquired as near-field images of the AWG output facet. The numerical aperture of the beams emerging from the AWG is approximately 0.22, therefore a microscope objective with  $NA \geq 0.22$  must be used to avoid vignetting of the beam. Due to the Rowland-geometry of the AWG devices, the focus of the output beam is located on a Rowland-circle which intersects the flat polished facet at the edges of the spectral image region. Defocus aberration at the output facet results in spectral resolution imbalance between the edges and the centre of the image plane, whereby the central region defines the minimum spectral resolution of the AWG.

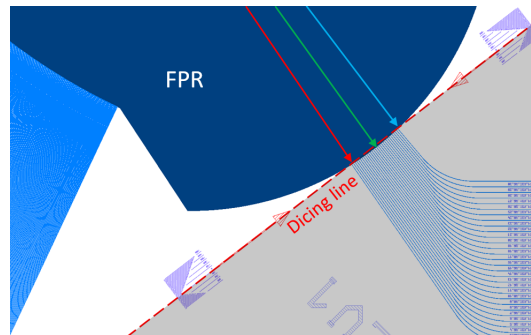


Fig. 20. Dicing scheme of the output facet (shown for type E AWG design). Blue, green and red arrows indicate the focused beam locations for shorter and longer wavelengths.

In order to fully remove the output waveguides, the output facets of the AWGs were diced and polished  $38 \mu\text{m}$  and  $47 \mu\text{m}$  beyond the Rowland circle for type C and type E AWGs, respectively, resulting in  $1390 \mu\text{m}$  and  $1625 \mu\text{m}$  wide flat facets. The dicing and polishing procedure was performed at Enablance USA Components. The imaging properties of the processed AWG devices were studied using an imaging system consisting of a Xenix InGaAs NIR camera and a microscope objective lens arranged along a single optical axis. Near field images of the AWG output facets were captured in a wavelength range equal to the  $FSR$  of each AWG, tuning the

TLS wavelength in discrete steps of 0.5 nm. Due to the restricted field of view (FOV) of the microscope objective, only 1/6 of the output facet could be covered by a single exposure, for which reason the camera and objective were moved parallel to the AWG facet to capture the region of interest. Optimal focus was achieved by minimizing the spot size in the vertical direction perpendicular to the plane of the FPR.

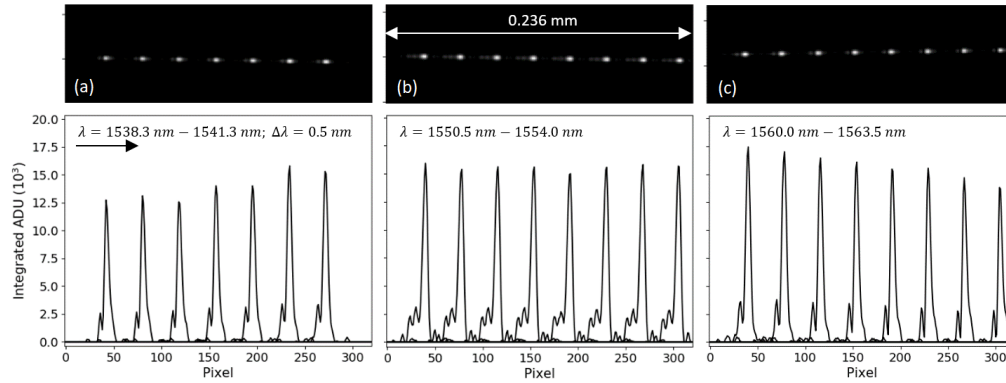


Fig. 21. Near field images of the diced output facet of AWG type C. Images taken at the edges (a, c) and centre of the facet (b). The arrow on the left side indicates the direction of increasing wavelength.

The results of the diced facet imaging for AWG type C are shown in Figure 21. The figure shows three selected segments of the AWG facet: short-wavelength and long-wavelength edges and the central region. Each segment shows a superposition of near field images taken in 0.5 nm wavelength increments. The images on the top show the AWG facets as seen by the camera. Vertical integration of columns was used to process the 2D camera images into 1D vertical slices, shown in the plots below the images. The intensity distributions show phase-error induced sidelobes reaching 20% of the main peak maximum. The averaged FWHM of the peaks at the centre of the AWG facet was determined as  $4.42 \mu\text{m}$  and the wavelength-dependent lateral peak shift was determined as  $56.3 \mu\text{m}/\text{nm}$ . A spectral resolving power of  $R = 19,600$  in the central region of the AWG facet was estimated from the measurement. Similarly, the average peak FWHM was determined as  $4.09 \mu\text{m}$  and  $4.0 \mu\text{m}$  at the short wavelength and long wavelength ends of the facet, respectively, resulting in a spectral resolving power estimate of  $R = 21,200$  and  $R = 21,900$  at the edges of the spectral image. The reduction of the spectral resolving power towards the centre of the AWG facet is expected due to defocus aberration of the Rowland grating geometry.

The interference image of the diced type E AWG was studied in a similar way using the same experimental setup configuration. Figure 22 shows superimposed near field images in the short-wavelength, central and long-wavelength sections of the output facet. While the interference peaks are free of sidelobes, a strong broadening due to defocus aberration can be observed in the central segment of the output facet, indicated by the elongation of the focal spot in horizontal direction. Image analysis shows a wavelength-dependent peak shift of  $28.5 \mu\text{m}/\text{nm}$ . The peak FWHM varies from  $3.9 \mu\text{m}$  at the short wavelength edge between  $1526.3 \text{ nm}$  and  $1533.3 \text{ nm}$  to  $8.47 \mu\text{m}$  in the central region between  $1551.3 \text{ nm}$  and  $1558.8 \text{ nm}$ . Accordingly, the spectral resolving power varies between  $R = 5,215$  in the central region of the image plane and  $R = 11,320$  at the short-wavelength edge. Figure 23 shows the variation of measured resolving power for both diced AWG devices on a normalized wavelength axis within the main spectral order. Minimum resolving powers of  $5,215$  (type E) and  $19,600$  (type C) have been achieved for Rowland-type AWG devices with a diced output image plane. The resolving power

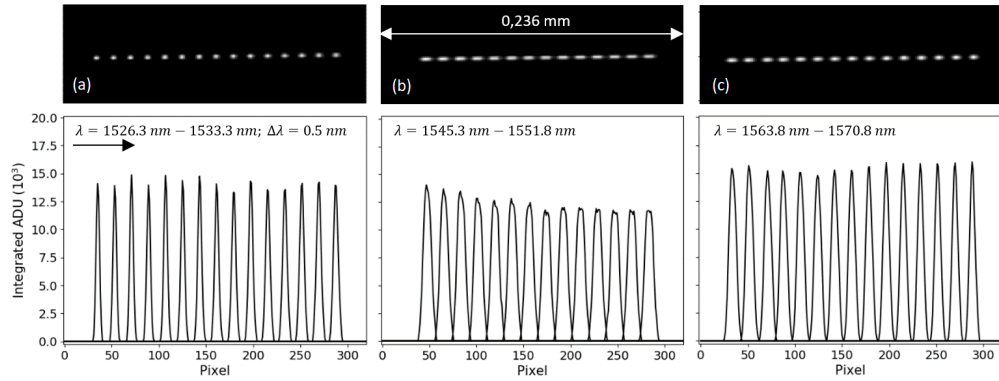


Fig. 22. Near field images of the diced output facet of AWG type E. Images taken at the edges (a, c) and centre of the facet (b). The arrow on the left side indicates the direction of increasing wavelength.

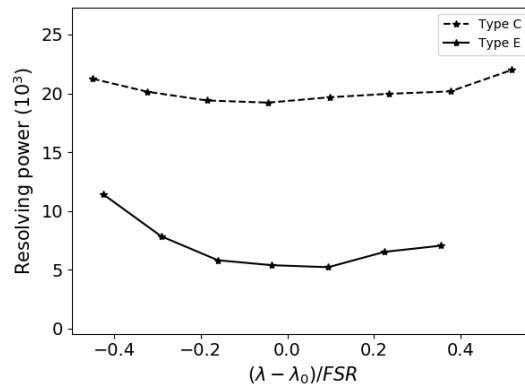


Fig. 23. Measured spectral resolving power of type C and type E AWG devices after dicing and polishing of the output facet.

non-uniformity was largest in the type E AWG device with a variation of  $> 50\%$  between the edges and the centre of the image plane.

Defocus after dicing was much weaker than expected theoretically for design C, varying only by  $10.5\%$  between the edge and centre of the output facet. Furthermore, the resolving power measured by direct imaging was higher than the estimate from the transmission measurement in section 7.1. This unexpected observation can be explained by distortion of the output beam due to fabrication related optical length errors of the waveguide array. We have used a Monte-Carlo method similar to the approach introduced in [23] to fit a model of the AWG to the measured transmission curve (see Figure 17) by random variation of the optical lengths of the array waveguides and minimization of the residual sum of squares between the model output and the measured data. After including the fitted data into the AWG simulation, we observed a very similar qualitative behaviour as seen in the experiment. In the simulation of the diffraction image at the centre of the polished facet including the fitted path length errors, the FWHM of the intensity peak increased from  $3.62 \mu\text{m}$  in the spot of maximum focus at  $z = 0 \mu\text{m}$  relative to the Rowland circle to  $3.89 \mu\text{m}$  at a location  $38 \mu\text{m}$  below, resulting in a resolving power of 22,400. In contrast, the simulated FWHM increased from  $2.91 \mu\text{m}$  at  $z = 0 \mu\text{m}$  to  $7.64 \mu\text{m}$  at  $z = 38 \mu\text{m}$  in the ideal AWG with perfectly tuned path lengths. Simulations of output channel transmission

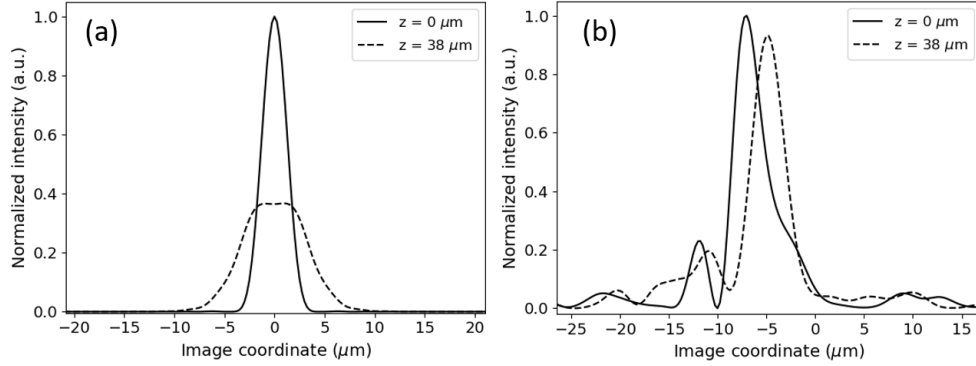


Fig. 24. Simulated defocus of the image on the output facet of AWG device C 38  $\mu\text{m}$  below the Rowland circle at 1550 nm. (a) Ideal AWG without path length errors. (b) Fitted model of fabricated device C.

bandwidth of the fitted model almost exactly matched the measured 3-dB bandwidth of 0.09 nm, corresponding to  $R = 17, 130$ . Figure 24 shows a comparison of defocus behaviour of an ideal AWG of type C with the simulated defocus behaviour of the fabricated AWG.

The near field imaging results show that defocus aberration is a significant performance limiting factor. The problem of defocus aberration is solved in the three-stigmatic-point AWG design [24], which is particularly essential for spectroscopy applications. The three-stigmatic-point method modifies the shape of the FPR as well as the lengths of the array waveguides to produce AWG designs with a flat image-plane and minimal aberrations in compliance with the requirements of astronomical spectrographs utilizing cross-dispersion. We will present a detailed theoretical and experimental analysis of three-stigmatic-point silica AWG devices in part II of our series.

In the next step, we have studied the polarization sensitivity of the diced AWGs by comparing images of interference peaks taken with TE and TM-polarized input light. Although the waveguide core design aims to minimize geometrical waveguide birefringence, the presence of stress-induced birefringence cannot be ruled out. In order to measure the polarization-dependent peak shift in the image plane, we took images at several wavelengths near  $\lambda_0 = 1550 \text{ nm}$  with purely TE-polarized light and repeated the procedure for the same set of wavelengths with purely TM-polarized light. The superimposed measurement results for type C and type E AWG are shown in Figure 25. Figure 25(a) shows the results for type C AWG. The images were taken in wavelength steps of 0.1 nm. A strong polarization-dependent shift of the image can be observed. For the type C AWG, we obtain  $PD\lambda = 0.04 \text{ nm}$ , indicating a waveguide array birefringence  $\Delta n_{\text{eff}} = n_{\text{eff,TE}} - n_{\text{eff,TM}} = 3.77 \times 10^{-5}$ . Similarly, we obtain  $PD\lambda = 0.026 \text{ nm}$  for the type E AWG, which corresponds to a waveguide birefringence  $\Delta n_{\text{eff}} = 2.45 \times 10^{-5}$ . The  $PD\lambda$  measured in our experiment is comparable to the value of 0.05 nm achieved using polarization compensation by core width adjustment in 2.5% silica waveguides [25]. However, a birefringence of the order  $10^{-5}$  is still significant considering the high spectral resolution targeted by the AWG designs. Improvement of the AWG designs with regard to polarization sensitivity is subject of future development work. Possible methods of birefringence cancellation in AWGs are described in [26–28]. Birefringence cancellation methods based on an angled star coupler geometry or waveguide core width variation are of special interest, as they avoid the post processing and losses introduced by the polyamide half-wave plate method. However, these methods require precise a-priori knowledge of the waveguide birefringence in the fabricated device.

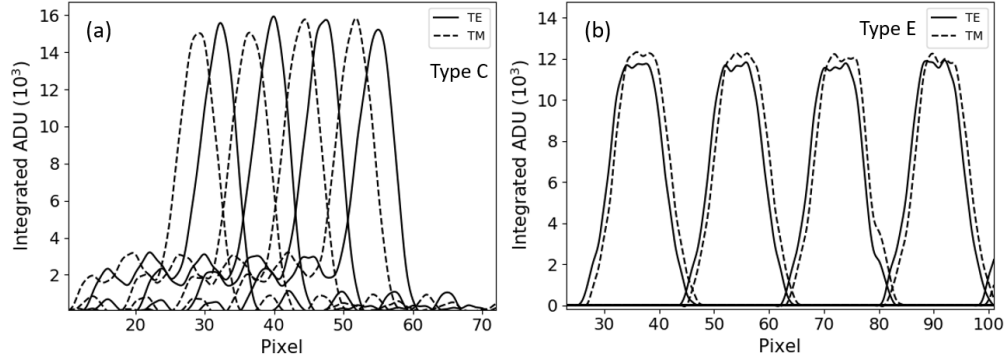


Fig. 25. Polarization dependent shift of the image near 1550 nm. (a) Type C: images taken in wavelength increments of 0.1 nm. (b) Type E: images taken in wavelength increments of 0.5 nm.

## 8. Conclusion

In the first part of a series of papers, we have presented an experimental study on the practical feasibility of high-resolution ( $R = \lambda/\Delta\lambda = 15,000\text{--}60,000$ ) arrayed waveguide gratings for use in near-infrared spectroscopy. In this study, we have used numerical modeling to develop a set of custom AWG designs, denoted A-E, on a 2% refractive index silica-on-silicon platform for operation in a region of the astronomical H-band covering 1500 nm - 1700 nm. High-spectral-order AWGs with a narrow free spectral range of 16 nm as well as low-order AWGs covering up to 48 nm were designed and characterized.

Output channel transmission spectrum measurements showed increasing degradation of AWG performance with increasing number of waveguides and average waveguide array length due to fabrication-related phase errors. The designs with foot-prints between  $4.8\text{ cm}^2$  and  $16.38\text{ cm}^2$  achieved spectral resolving powers between 10,333 and 18,900, estimated from the 3-dB-bandwidth of the output channel transmission, whereby the highest resolution was observed in the smallest design. Increasing the spectral resolution significantly beyond  $\sim 20,000$  by increasing the focal length and number of waveguides proved to be impractical, as the theoretical benefit was surpassed by degradation due to phase errors. Fabricated AWG devices of type C and E were selected for further processing into spectroscopic AWGs by removal of the output waveguides and polishing of the chip facet to optical quality. The interference maximum on the polished output facet was directly imaged with a high-NA microscope objective and a NIR camera, using polarization control for TE and TM measurements. Spectral resolving powers of  $R \geq 19,600$  (type C) and  $R \geq 5,215$  (type E) were measured by analysis of the camera images. As expected from AWGs of the Rowland-type, the resolving power was non-uniform across the image plane due to defocus aberration on the flat polished facet and varied by 10.5% in device C and 54.4% in device E. The anomalously small defocus in device C was shown to be caused by phase errors in a numerical simulation of the fabricated device.

Measurements of polarization sensitivity showed a significant  $\text{PD}\lambda$  of 0.04 nm for type C and 0.026 nm for type E. Taking into account the device geometry, a birefringence of  $\Delta n_{\text{eff}} = 2.45 \times 10^{-5}$  was estimated.

In summary, we have demonstrated the feasibility of custom-developed spectroscopic AWGs achieving spectral resolving powers of up to  $R = 20,000$  without additional post processing, such as phase error correction by UV trimming [29]. However, we have observed rapid degradation of performance beyond this limit, as phase error induced cross-talk rendered devices with a target resolving power  $R \geq 30,000$  practically dysfunctional. We conclude from this result the necessity

of phase error compensation in high-resolution spectroscopic AWGs. Interferometric methods of phase error measurement in AWGs are described in the literature [30, 31]. Material systems other than silica on silicon, such as InP, potentially allow for dynamic phase error correction [32]. The presented results show the performance-limiting effect of defocus aberration in Rowland-type AWGs. Therefore, we propose implementations of low-aberration three-stigmatic-point geometries in all future generations of spectroscopic AWGs for astronomy. The third major issue is polarization sensitivity of the waveguide array, which can be addressed by modification of the waveguide core geometry. These three outlined challenges are essential for future high-performance AWG-based astronomical instruments. The Potsdam Arrayed Waveguide Spectrograph (PAWS), a full cross-dispersion AWG spectrograph demonstrator with Teledyne H2RG detector is currently being developed in Potsdam to test the first generation of AWGs as well as future devices on sky [13]. The system will encompass a cryostat in order to minimize thermal radiation in the wavelength range of operation as well as the dark current of the image detector, which is essential for long-exposure observations under photon-starved conditions.

**Funding.** This work is supported by the BMBF project “Meta-ZIK Astrooptics” (grant No. 03Z22A511).

**Acknowledgments.** This work is supported by the BMBF project “Meta-ZIK Astrooptics” (grant No. 03Z22A511).

We gratefully acknowledge the assistance of Dele Zhu, Vadim Makan, Dr. Julia Fiebrandt and Dr. Ziyang Zhang. We especially thank Prof. Dr. Martin Schell, Fraunhofer HHI, Berlin, for sharing general thoughts and providing helpful advice.

**Disclosures.** The authors declare no conflicts of interest.

**Data availability.** Data underlying the results presented in this paper are not publicly available at this time but may be obtained from the authors upon reasonable request.

## References

1. P. Ferruit, G. Bagnasco, R. Barho, S. Birkmann, T. Böker, G. D. Marchi, B. Dorner, R. Ehrenwinkler, M. Falcolini, G. Giardino, X. Gnata, K. Honnen, P. Jakobsen, P. Jensen, M. Kolm, H.-U. Maier, R. Maurer, M. Melf, P. Mosner, P. Rumler, J.-C. Salvignol, M. Sirianni, P. Strada, M. te Plate, and T. Wettemann, “The JWST near-infrared spectrograph NIRSpec: status,” in *Space Telescopes and Instrumentation 2012: Optical, Infrared, and Millimeter Wave*, vol. 8442 M. C. Clampin, G. G. Fazio, H. A. MacEwen, and J. M. O. Jr., eds., International Society for Optics and Photonics (SPIE, 2012), pp. 984 – 992.
2. H. Kaeuß, P. Ballester, P. Biereichel, B. Delabre, R. Donaldson, R. Dorn, E. Fedrigo, G. Fischer, F. Franza, D. Gojak, G. Huster, Y. Jung, J.-L. Lizon, L. Mehrgan, M. Meyer, A. Moorwood, J.-F. Pirard, J. Paufigue, and S. Wegerer, “CRIRES: a high-resolution infrared spectrograph for ESO’s VLT,” *Proc. SPIE* **5492** (2004).
3. J. Bland-Hawthorn and A. Horton, “Instruments without optics: An integrated photonic spectrograph,” *Proc SPIE* **6269** (2006).
4. N. Cvetojevic, J. S. Lawrence, S. C. Ellis, J. Bland-Hawthorn, R. Haynes, and A. Horton, “Characterization and on-sky demonstration of an integrated photonic spectrograph for astronomy,” *Opt. Express* **17**, 18643–18650 (2009).
5. N. Cvetojevic, N. Jovanovic, C. Betters, J. Lawrence, S. Ellis, G. Robertson, and J. Bland-Hawthorn, “First starlight spectrum captured using an integrated photonic micro-spectrograph,” *Astron. Astrophys.* **544** (2012).
6. P. Gatkine, S. Veilleux, Y. Hu, J. Bland-Hawthorn, and M. Dagenais, “Arrayed waveguide grating spectrometers for astronomical applications: new results,” *Opt. Express* **25**, 17918–17935 (2017).
7. M. K. Smit, “New focusing and dispersive planar component based on an optical phased array,” *Electron. Lett.* **24**, 385–386 (1988).
8. H. Takahashi, S. Suzuki, K. Kato, and I. Nishi, “Arrayed-waveguide grating for wavelength division multi/demultiplexer with nanometre resolution,” *Electron. Lett.* **26**, 87–88 (1990). Copyright: Copyright 2017 Elsevier B.V., All rights reserved.
9. C. Dragone, “An  $N \times N$  optical multiplexer using a planar arrangement of two star couplers,” *IEEE Photonics Technol. Lett.* **3**, 812–815 (1991).
10. K. Okamoto, *Fundamentals of Optical Waveguides* (Academic Press, 2006).
11. X. J. M. Leijtens, B. Kuhlrow, and M. K. Smit, *Arrayed Waveguide Gratings* (Springer Berlin Heidelberg, Berlin, Heidelberg, 2006), pp. 125–187.
12. P. Muñoz, D. Pastor, and J. Capmany, “Modeling and design of arrayed waveguide gratings,” *Light. Technol. J.* **20**, 661–674 (2002).



13. E. Hernandez, A. Stoll, S.-M. Bauer, A. Berdja, R. Bernardi, C. Guzmán, A. Günther, K. Madhav, M. Roth, C. Sandin, and C. Villanueva, "Optomechanical design of PAWS, the potsdam arrayed waveguide spectrograph," in *SPIE Vol. 11451*, (2020), p. 193.
14. P. Gatkine, S. Veilleux, Y. Hu, J. Bland-Hawthorn, and M. Dagenais, "Towards a multi-input astrophotonic AWG spectrograph," in *Advances in Optical and Mechanical Technologies for Telescopes and Instrumentation III*, vol. 10706 R. Navarro and R. Geyl, eds., International Society for Optics and Photonics (SPIE, 2018), pp. 1487 – 1494.
15. F. Watson, "Multifiber waveguide spectrograph for astronomy?" in *Defense, Security, and Sensing*, (1995).
16. A. Stoll, K. Madhav, and M. Roth, "Performance limits of astronomical arrayed waveguide gratings on a silica platform," *Opt. Express* **28**, 39354–39367 (2020).
17. P. Gatkine, N. Jovanovic, C. Hopgood, S. Ellis, R. Broeke, K. Ławniczuk, J. Jewell, J. K. Wallace, and D. Mawet, "Potential of commercial SiN MPW platforms for developing mid/high-resolution integrated photonic spectrographs for astronomy," *Appl. Opt.* **60**, D15–D32 (2021).
18. A. Stoll, Z. Zhang, R. Haynes, and M. Roth, "High-resolution arrayed-waveguide-gratings in astronomy: Design and fabrication challenges," *Photonics* **4** (2017).
19. K. Wörhoff, R. G. Heideman, A. Leinse, and M. Hoekman, "TriPleX: a versatile dielectric photonic platform," *Adv. Opt. Technol.* **4**, 189–207 (2015).
20. M. D. Feit and J. A. Fleck, "Computation of mode properties in optical fiber waveguides by a propagating beam method," *Appl. Opt.* **19**, 1154–1164 (1980).
21. W. K. Burns, A. F. Milton, and A. B. Lee, "Optical waveguide parabolic coupling horns," *Appl. Phys. Lett.* **30**, 28–30 (1977).
22. H. Takahashi, K. Oda, H. Toba, and Y. Inoue, "Transmission characteristics of arrayed waveguide  $N \times N$  wavelength multiplexer," *J. Light. Technol.* **13**, 447–455 (1995).
23. Y.-H. Oh, S.-W. Lim, and C.-S. Go, "Alternative method of awg phase measurement based on fitting interference intensity," *J. Opt. Soc. Korea* **16**, 91–94 (2012).
24. Daoyi Wang, Guofan Jin, Yingbai Yan, and Minxian Wu, "Aberration theory of arrayed waveguide grating," *J. Light. Technol.* **19**, 279–284 (2001).
25. K. Maru, M. Okawa, Y. Abe, T. Hakuta, S. Himi, and H. Uetsuka, "Silica-based 2.5%- $\delta$  arrayed waveguide grating using simple polarisation compensation method with core width adjustment," *Electron. Lett.* **43**, 26 – 27 (2007).
26. Y. Inoue, H. Takahashi, S. Ando, T. Sawada, A. Himeno, and M. Kawachi, "Elimination of polarization sensitivity in silica-based wavelength division multiplexer using a polyimide half waveplate," *J. Light. Technol.* **15**, 1947–1957 (1997).
27. Y. Inoue, M. Itoh, Y. Hashizume, Y. Hibino, A. Sugita, and A. Himeno, "Novel birefringence compensating AWG design," OFC 2001. Opt. Fiber Commun. Conf. Exhib. Tech. Dig. Postconf. Ed. (IEEE Cat. 01CH37171) **3**, WB4–WB4 (2001).
28. T. Lang, J.-J. He, J.-G. Kuang, and S. He, "Birefringence compensated AWG demultiplexer with angled star couplers," *Opt. express* **15**, 15022–8 (2007).
29. D. A. Zauner, J. Hubner, K. J. Malone, and M. Kristensen, "UV trimming of arrayed-waveguide grating wavelength division demultiplexers," *Electron. Lett.* **34**, 780–781 (1998).
30. K. Takada and K. Okamoto, "Frequency-domain measurement of phase error distribution in narrow-channel arrayed waveguide grating," *Electron. Lett.* **36**, 160–161 (2000).
31. K. Takada and S. ichi Satoh, "Method for measuring the phase error distribution of a wideband arrayed waveguide grating in the frequency domain," *Opt. Lett.* **31**, 323–325 (2006).
32. W. Jiang, N. Fontaine, F. Soares, J. Baek, K. Okamoto, S. Yoo, F. Olsson, and S. Lourduodoss, "Dynamic phase-error compensation for high-resolution InP arrayed-waveguide grating using electro-optic effect," in *Lasers and Electro-Optics Society Annual Meeting-LEOS*, (2008), pp. 53 – 54.